Fractal Analysis of Bone X-Ray Tomographic Microscopy Projections

Rachid Jennane*, William J. Ohley, *Member, IEEE*, Sharmila Majumdar, and Gérald Lemineur

***Abstract*—Fractal analysis of bone X-ray images has received much interest recently for the diagnosis of bone disease. In this paper, we propose a fractal analysis of bone X-ray tomographic microscopy (XTM) projections. The aim of the study is to establish whether or not there is a correlation between three–dimensional (3-D) trabecular changes and two-dimensional (2-D) fractal descriptors. Using a highly collimated beam, 3-D bone X-ray tomographic images were obtained. Trabecular bone loss was simulated using a mathematical morphology method. Then, 2-D projections were generated in each of the three orthogonal directions. Finally, the model of fractional Brownian motion (fBm) was used on bone XTM 2-D projections to characterize changes in bone structure that occur during disease, such a simulation of bone loss. Results indicate that fBm is a robust texture model allowing quantification of simulations of trabecular bone changes.**

***Index Terms*—Fractal analysis, projection, trabecular bone characterization, XTM.**

I. Introduction

OSTEOPOROSIS is characterized by a decrease in both bone mass and strength. This disease occurs with aging or during menopause. It can result in an increase risk of fractures [1], [2]. Many techniques can be used to determine bone mass or bone density. However this property may not always represent the effective strength. Bone strength is also dependent upon trabecular bone micro-architecture. Characterization of the structural and physical properties of trabecular bone (architecture) appears to be an important adjunct in determining fracture risk with greater accuracy [3]. Architectural parameters include trabecular porosity, the density of intertrabecular connections, the arrangement, and the orientation of trabeculae [4]. Histomorphometry, the reference technique for analysis of trabecular architecture, requires bone biopsy and cannot be used on a large scale.

Trabecular bone micro-architecture is recognized as an important factor for the determination of bone strength. Bone density remains the main factor of bone strength, but its reduction is not the sole factor involved in bone fragility of osteoporosis. Measurements of bone mass [5] or volume [6] show a considerable overlap between osteoporosis and control subjects. A structural evaluation of the trabecular micro-architecture and its changes allows better understanding of the pathophysiologic events that characterize bone aging and osteoporosis. This evaluation, if we consider noninvasive procedures, remains a difficult task. Therefore, it would be very useful if these changes could be measured with noninvasive techniques, such as radiographs, and to assess the status of the bone by analysis of the fractal organization.

Due to its simplicity, radiographs have been used for several years [7], [8] especially by use of a fractional Brownian motion (fBm) model to access trabecular organization [9], [10]. An X-ray radiograph of a bone is a two-dimensional (2-D) projection of a three–dimensional (3-D) complex structure. The resulting image usually appears as a nonhomogeneous, anisotropic and textured image. The problem in many applications of fractals to such 2-D projections of 3-D complex structures is in exactly how the main Hurst (H) parameter, of fBm is related to the development of osteoporosis.

Recent imaging techniques, such as microcomputed tomography [11], micromagnetic resonance imaging [12], optical serial reconstruction [13], and X-ray tomographic microscopy (XTM) [14] produce 3-D images of trabecular bone. These images allow 3-D morphology measurements and can be used to describe the microstructure of trabecular bone.

In this paper, we seek to determine the relationship between the loss of trabecular bone elements and the corresponding fBm parameter H. Thus, it is an attempt to answer the question of what H measures. A perfect experiment would be to have high-resolution images of a particular bone segment as it undergoes the natural osteoporosis process. With both 3-D images and the corresponding X-ray image, we could apply the fBm model and produce a direct correlation between the H of fBm and the osteoporosis process. However, this is difficult at present, since the radiation required to produce 3-D images is not compatible with life. Failing this availability, in this study we examine high-resolution XTM images and apply numerical techniques to simulate both trabecular bone loss and the 2-D X-ray process. The aim is not to entirely model the projection process but to evaluate precisely 3-D micro-architectural bone changes that occur during diseases using the fBm model on 2-D bone projections.

The paper is organized as follows: Section II discusses the properties of fBm. Section III deals with the X-ray tomographic images. Simulation of trabecular bone loss and the 2-D image projections are illustrated in Section IV. Section V presents fractal analysis results and bone architecture measures. Finally, we conclude with a brief discussion of this work.

Manuscript received May 17, 1999; revised February 10, 2001. The Associate Editor responsible for coordinating the review of this paper and recommending its publication was A. Manducz. *Asterisk indicates corresponding author.*

*R. Jennane is with the Laboratory of Electronics, Signals and Images, University of Orleans, BP 6744, 45067 Orleans, France (e-mail: Rachid.Jennane@univ-orleans.fr).

W. J. Ohley is with the Electrical Engineering Department, University of Rhode Island, Kingston, RI 02881 USA.

S. Majumdar is with the Magnetic Resonance Science Center, University of California, San Francisco, CA 94143 USA.

G. Lemineur is with the Laboratory of Electronics, Signals and Images, University of Orleans, 45067 Orleans, France.

Publisher Item Identifier S 0278-0062(01)04407-X.

II. Fractional Brownian Motion and Fractional Gaussian Noise

The model of fBm introduced by Mandelbrot and Van Ness [15] has been shown to be useful in a wide variety of natural phenomena. These processes belong to the class of self-similar and nonstationary processes which possess many interesting properties and have received much attention in recent years. In this section, we define this process and discuss some of its interesting properties. A more complete overview is given in [15]. The FBm process, denoted $B_H(t)$, where t is a time index, is a nonstationary stochastic Gaussian process, with zero mean and is mainly described by a single parameter$H$, related to the fractal dimension, D

$$D = E + 1 - H \tag{1}$$

where E corresponds to its Euclidean dimension and H, is called the Hurst coefficient $(0 < H < 1)$. The smaller H is, the greater is the statistical roughness of the path.

The nonstationarity of fBm makes analysis difficult. However, the increments of fBm are a strict sense stationary process, which has been termed fractional Gaussian noise (fGn). Many of the properties of fGn have been stated in [15]. Briefly, we can summarize as follows. FGn is a Gaussian, zero mean, and stationary stochastic process, referred to as $G_{H,m}$ if m is a discrete time interval. It is defined by

$$G_{H,m}(n) = B_H(n+m) - B_H(n), \quad \text{with } n, m \in \mathbb{N} \tag{2}$$

where m is a discrete time interval and $\mathbb{N}$ is the set of the natural numbers.

A number of fBm analysis methods exist but most of them take into account only a part of fBm properties. In a previous study, eight estimators of the H parameter were compared [16] using reference fBm signals [17]. Only three methods gave acceptable results. Of these, the maximum likelihood estimator (MLE) provided the most accurate estimate with the lowest bias and a variance close to the Cramer–Rao bound [18]. The MLE has a series of asymptotic properties [19] which have contributed to generalizing its use in signal processing.

The MLE was applied to compute the H parameter of each image using a numerical method[20]. This analysis was done line-by-line on each image. 200 estimation values of H were obtained on lines of 200 pixels length, their mean and standard deviation were evaluated for each image.

A theoretical 2-D MLE can be derived. Its use would necessitate an inversion of a tensor which poses computational problems. In fact, the covariance matrix of the process increments has to be inverted for many trial values. This can be costly in terms of CPU time and memory consumption, in particular if the dimension of data is high. This inversion can be simplified [21] by taking advantage of its special Toeplitz-Block structure. However, its application is limited to small images, and as other investigations have shown [22], using the line-to-line analysis can yield useful image descriptors.

III. X-Ray Tomographic Microscopy (XTM)

Seven frozen human distal radii were used to derive a total of seven cubic specimens of trabecular bone. The cubic sections were cut under constant irrigation using a precision diamond saw. Cubes were cut to a dimension of 12 mm and oriented with respect to the anatomic axes.

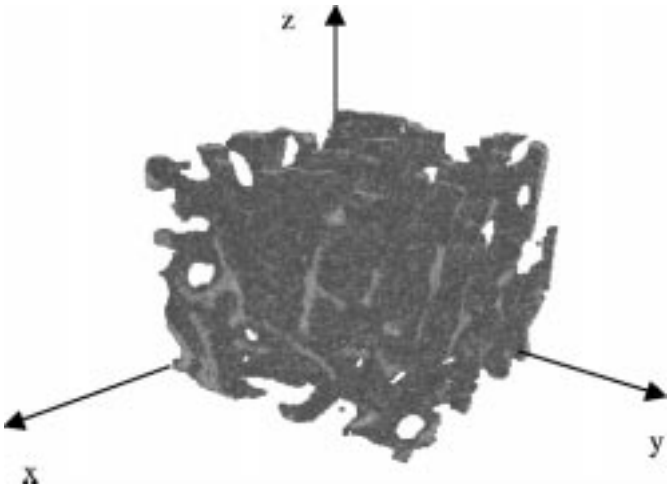

Fig. 1. The central 200 × 200 × 200 part of a 3-D reconstructed XTM image.

X-ray tomographic images were obtained using a highly collimated X-ray beam from the synchrotron source of the Stanford Synchrotron Radiation Laboratory. The radiation was monochromatic at $\sim$ 25 keV using a crystal silicon monochromator. A scintillator crystal and charge-coupled device detector were used to acquire the projections. Each specimen was placed on a rotating stage and projections at different angles were obtained, and each image was reconstructed using Fourier filtered back projection [23]. The central $6.5 \times 6.5 \times 6\ \text{mm}^3$ of each cube was imaged at an isotropic resolution of 17.6 μmm. Three sets of slices 2 mm each were obtained and concatenated to obtain the 6-mm slab. Each image set took approximately 30 min to acquire and 2 h to reconstruct off-line. The whole data set was too large to analyze, and we only used the central part of each image which is $3.52 \times 3.52 \times 3.52\ \text{mm}^3$ (Fig. 1). Fig. 2 shows several planes of the central $3.52 \times 3.52\ \text{mm}^2$ of such a cube.

IV. Simulation of Trabecular Bone Loss and X-Ray Projection

A. Simulation of Bone Loss

To simulate trabecular bone loss on our 3-D XTM images, a mathematical morphology method named *erosion* was used. Mathematical morphology as developed by Serra [24] is basically a set theory and uses set transformations for image analysis. It extracts the impact of a particular shape on images via the concept of a structuring element. Thus, the structuring element may be visualized as a probe that slides across the image, testing the spatial nature of the image at every point. The erosion transformation is popularly conceived of as a shrinking of the original image. The eroded image is often thought of as being contained in the original image.

If A denotes an image and B the structuring element, the erosion of A by B is denoted $A \Theta B$ and is defined by

$$A \Theta B = \bigcap_{b \in B} A - b = \{x : (B + x) \subseteq A\} \tag{3}$$

where $(B + x)$ denotes the translation of B by x. This says that the erosion of A by B is the set of all points x such that$B$,

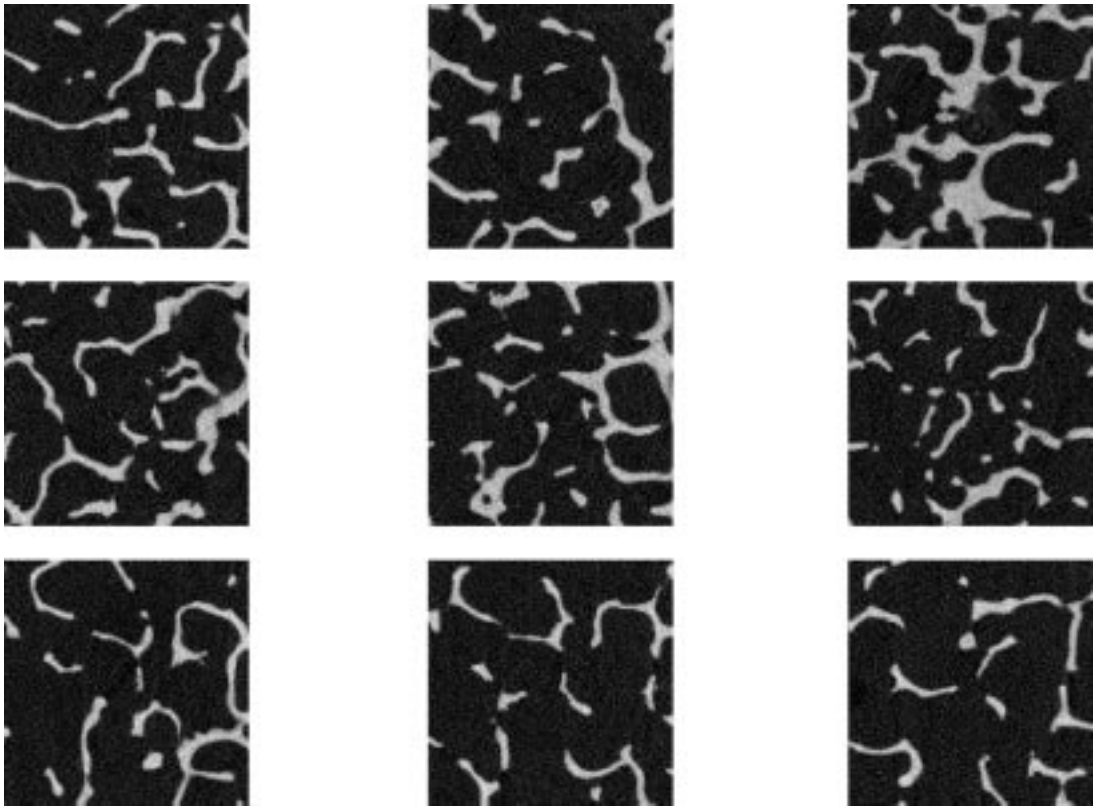

Fig. 2. Several planes of the central 200 × 200 × 200 part of the reconstructed XTM image. From top to bottom and left to right, every 20th section in the 3-D stack is displayed.

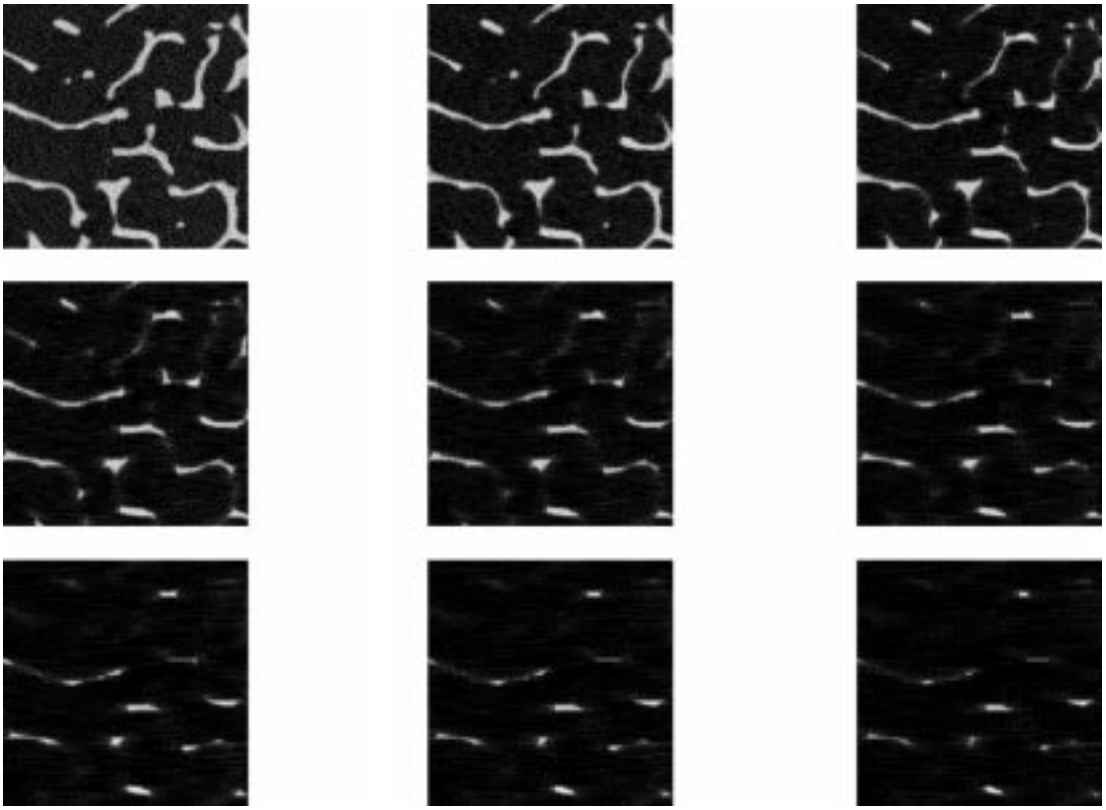

Fig. 3. From top to bottom and left to right, the central 200 × 200 pixels of an XTM image plane and the resulting images after $1, 2, \ldots, 8$ erosions.

translated by x, is contained in A. From the above expression, it can be seen that eroding by B removes from each border of the structure, parts smaller than B and also all the isolated structures smaller than B.

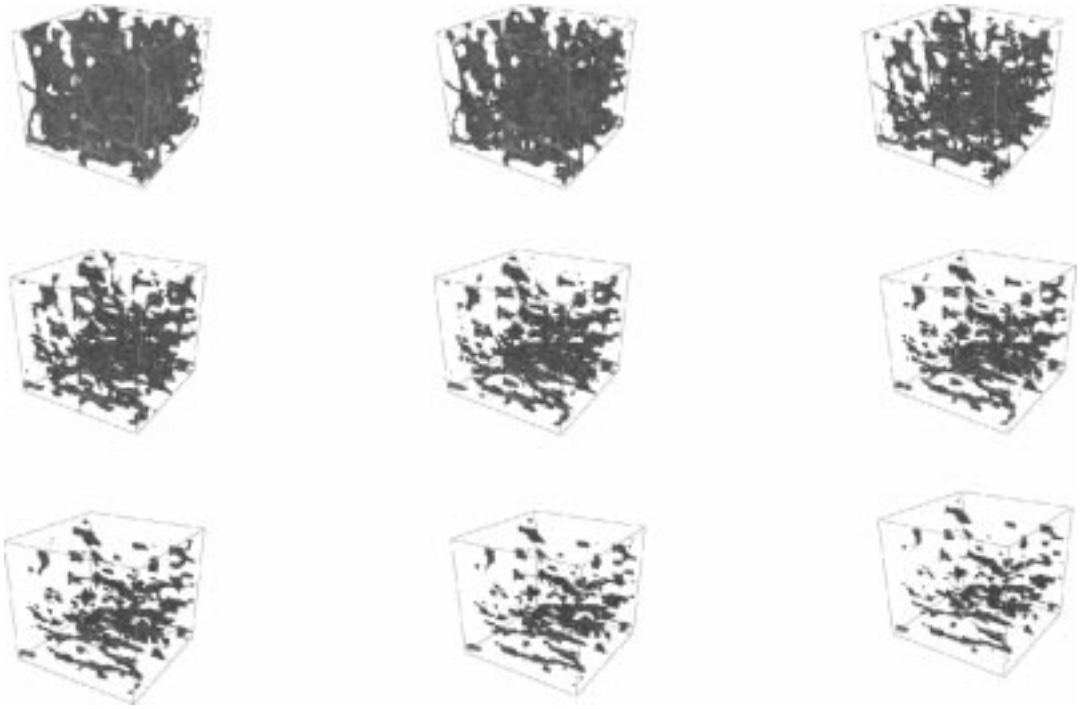

Fig. 4. From top to bottom and left to right, the central 200 × 200 × 200 part of an XTM image and the resulting 3-D images after $1, 2, \ldots, 8$ erosions.

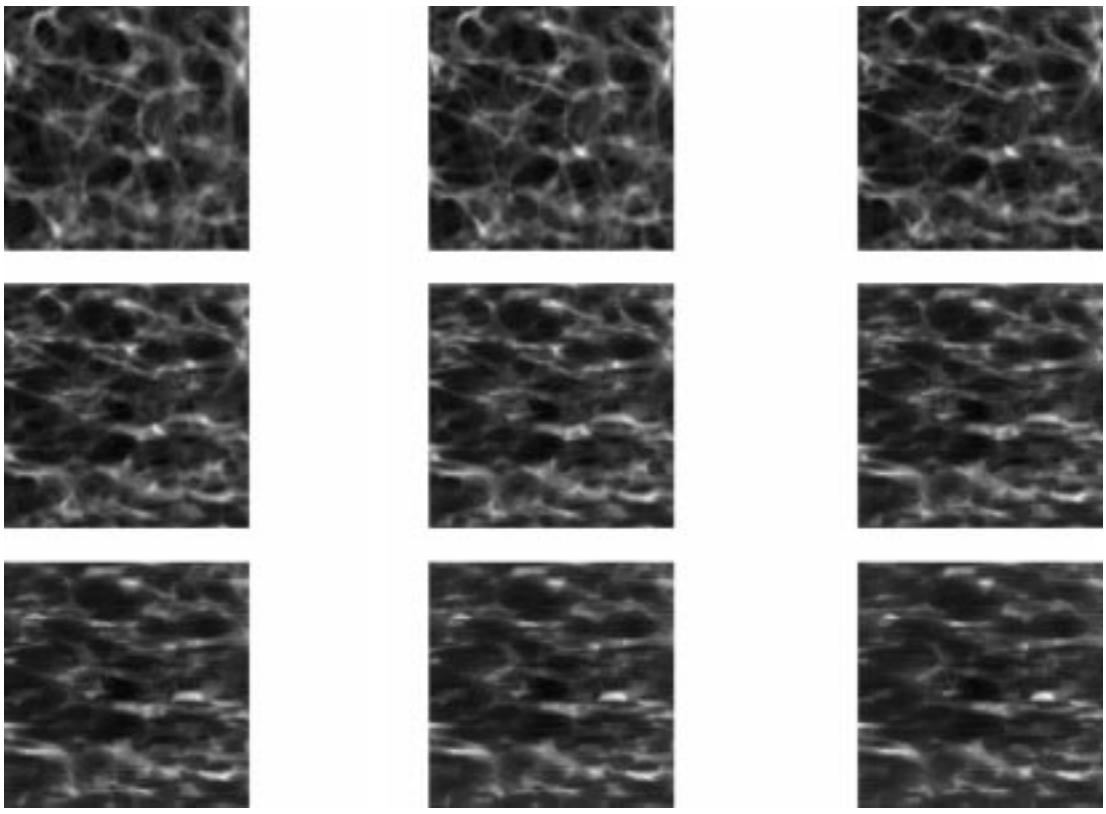

Fig. 5. From top to bottom and left to right, computed 2-D image projections after $0, 1, 2, \ldots, 8$ erosions.

A multivariate erosion of the image A by the structuring element B at scale $n = 0, 1, 2, \ldots$ is defined as

$$A \Theta n B = \underbrace{(A \Theta B) \Theta B \cdots \Theta B}_{n \text{ times}}. \tag{4}$$

This expression leads to different stages of trabecular bone removal. The technique permits modifying the bone micro-architecture leading to several models of bone structure. The above algorithm was used to compute trabecular bone loss on each plane. As a structuring element, $(1, 0, 0, 1)$ was used.

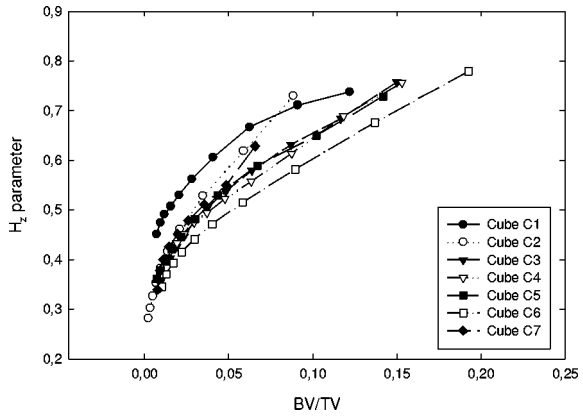

Fig. 6. Hurst coefficient (H_z) versus BV/TV computed for different z projections and bone structure models.

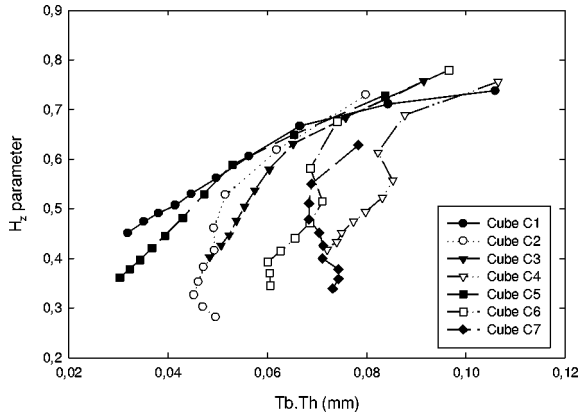

Fig. 7. H_z versus trabecular thickness (Tb.Th) computed for different z projections and bone structure models.

Fig. 3 shows a single bone cube plane and the effect of the erosion operations on its micro-architecture. As can be seen, this algorithm results in a loss of trabecular bone. Effects on the cubes are represented in Fig. 4.

B. Two-Dimensional Projection

In X-ray transmission radiography, the information from attenuation of X-rays as they pass through bone structure leads to the characterization of different tissues in the object. As an X-ray passes through an object, its intensity is changed depending on the object attenuation. The following analysis will not consider the general problem of generating an X-ray image of an object. Instead, it will be restricted to describing projections from a series of planes.

Let $f(x, y, z)$ be the function which represents the spatial distribution of the object. Then $p_\alpha(u, v)$ denotes an image projection defined as a line integral of the original 3-D image with parameters u and v defining the position on the detector and α being one of the three orthogonal image orientations (x, y, z)

$$p_\alpha(u,v) = \int_A f(x,y,z)d\alpha \quad \text{where } \alpha = x, y, \text{or } z. \qquad (5)$$

From a practical point of view, this definition can be generalized to the discrete time case, and (5) can be descretized by replacing the integral with a sum.

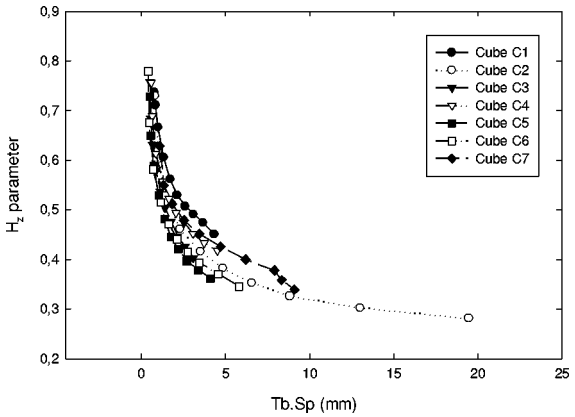

Fig. 8. H_z versus trabecular spacing (Tb.Sp) computed for different z projections and bone structure models.

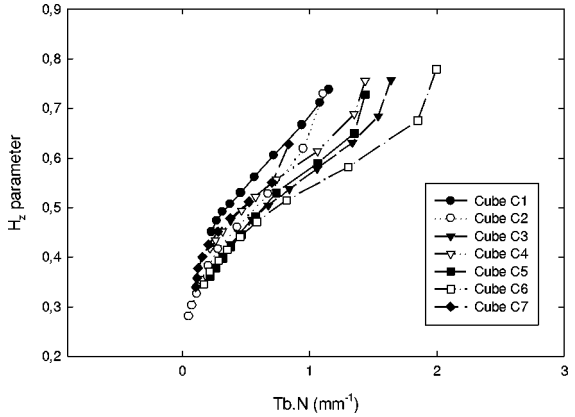

Fig. 9. H_z versus trabecular number (Tb.N) computed for different z projections and bone structure models.

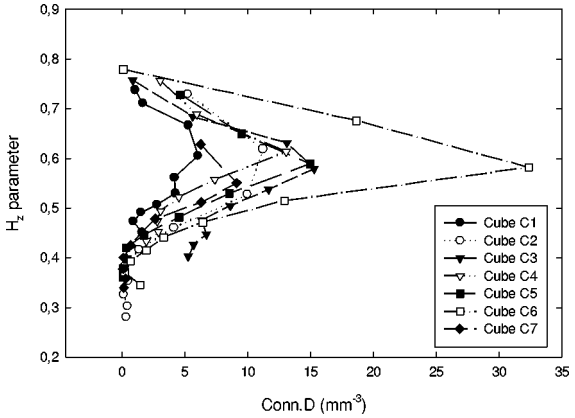

Fig. 10. H_z versus connectivity density (Conn.D) computed for different z projections and bone structure models.

In Fig. 5, the effects of the simulations of trabecular bone loss can be seen in the resulting 2-D image projections computed following (5) in the spatial domain.

V. Image Assessment and Results

Seven XTM images (C1–C7) were obtained following the protocol described in Section III. They were acquired as $z = 351$ planes of $x{*}y{*}8$ bit pixels with $(x, y) = (381, 381)$. To reduce time and memory consumption and because of erosion border

TABLE I
MEAN ± STANDARD DEVIATION (STD) FOR EACH 3-D PARAMETER COMPUTED ON THE ORIGINAL AND ERODED CUBES COMPARED TO THE MEAN ± STD OF THE H_x, H_y, AND H_z PARAMETERS COMPUTED ON THE CORRESPONDING PROJECTIONS

	H_x	H_y	H_z	BV/TV	Tb.Th mm	Tb.Sp mm	Tb.N mm^{-1}	Conn.D mm^{-3}
Stage0	0.970±0.012	0.904±0.029	0.731±0.049	0.131±0.043	0.092±0.012	0.673±0.243	1.410±0.400	3.013±2.416
Stage1	0.915±0.028	0.701±0.033	0.654±0.055	0.096±0.032	0.074±0.010	0.777±0.307	1.292±0.398	8.809±5.362
Stage2	0.848±0.045	0.600±0.036	0.589±0.055	0.066±0.024	0.065±0.010	1.035±0.441	1.016±0.320	13.577±9.04
Stage3	0.784±0.060	0.533±0.044	0.532±0.052	0.045±0017	0.063±0.013	1.499±0.648	0.725±0.246	8.131±4.578
Stage4	0.722±0.073	0.490±0.047	0.492±0.051	0.033±0.013	0.060±0.014	2.075±0.995	0.548±0.206	4.881±3.474
Stage5	0.665±0.083	0.459±0.046	0.460±0.051	0.025±0.011	0.058±0.015	2.727±1.430	0.432±0.173	3.126±2.817
Stage6	0.610±0.090	0.436±0.045	0.435±0.053	0.019±0.009	0.056±0.015	3.524±1.984	0.345±0.145	2.107±2.182
Stage7	0.558±0.096	0.414±0.043	0.412±0.055	0.015±0.007	0.054±0.016	4.461±2.713	0.282±0.124	1.772±2.386
Stage8	0.509±0.099	0.395±0.042	0.392±0.057	0.012±0.006	0.053±0.017	5.615±3.758	0.231±0.104	1.356±2.009
Stage9	0.462±0.101	0.376±0.041	0.371±0.057	0.010±0.005	0.052±0.017	7.207±5.742	0.191±0.089	1.538±1.804

effects we only used the central part of each cube $(x, y, z) =$ (200, 200, 200).

For each of the three orthogonal directions, to simulate bone loss, we realized n erosions$(1 \leq n \leq 9)$ on each cube. For each erosion step, an image projection was computed. Using the line-to-line MLE, each image was analyzed and the mean H parameter values were computed, refered to as H_x, H_y, and H_z for the x, y, and z orientations respectively.

Densitometric and architectural changes were evaluated on the 3-D images. The bone volume fraction (BV/TV) is a measure of the volume of trabecular bone (BV) per total volume (TV) of analysis in the cube. The trabecular thickness (Tb.Th) is a measure of the average thickness of the trabeculae. The trabecular separation (Tb.Sp) is a measure of the average distance between trabeculae. The trabecular number (Tb.N), is a measure of how many trabeculae there are in a specimen per unit volume. The connectivity density (Conn.D) gives a measure of how connected the material is.

At each step, BV/TV, Tb.Th, Tb.Sp, Tb.N, and Conn.D, were computed. For BV/TV, Tb.Th, Tb.Sp, and Tb.N we used the code referenced in [25] which analyzes a spherical test region from a 3-D image, with the analysis sphere defined by the user. For this study, a 3.52-mm sphere centered in the middle of the original cubes was used. For Conn.D, we implemented the method in [26] which uses the Euler characteristic for quantifying the connectivity of bone. Conn.D was computed as the zeroth betti number minus the Euler characteristic. Components with less than 300 pixels were not counted.

These 3-D densitometric and architectural indices were compared to the H parameters computed on 2-D projections. Results are presented on Figs. 6–10 for H_z versus BV/TV, Tb.Th, Tb.Sp, Tb.N, and Conn.D respectively.

Table I reports results expressed as mean ± standard deviation obtained using the estimated values BV/TV, Tb.Th, Tb.Sp, Tb.N and Conn.D computed on the original and the eroded cubes at different stages compared to H_x, H_y, H_z computed on the different projections. As demonstrated on Table II, there was a significant correlation between (H_x, H_y, H_z) and (BV/TV, Tb.Th, Tb.Sp, Tb.N). A poor relationship was found between (H_x, H_y, H_z) and Conn.D due essentially to the morphological tool (erosion) used to compute trabecular bone loss. As can be seen on Fig. 4, at the first stages, the erosion introduces small cavities in the structure, then pieces of trabecular bone are completely isolated from the main structure. This gives disconnected trabeculae which are not taken in consideration for computing Conn.D.

TABLE II
MEAN ± STD FOR CORRELATION COEFFICIENTS COMPUTED ON (H_x, H_y, AND H_z) AND (BV/TV, TB.TH, TB.SP, TB.N, AND CONN.D)

	BV/TV	Tb.Th	Tb.Sp	Tb.N	Conn.D
H_x	0.925±0.021	0.727±0.391	-0.953±0.041	0.967±0.013	0.563±0.279
H_y	0.991±0.007	0.858±0.317	-0.788±0.069	0.956±0.015	0.316±0.397
H_z	0.982±0.011	0.807±0.351	-0.881±0.055	0.991±0.006	0.461±0.341

As evidenced by these results, there is a clear decrease in H parameters while the trabecular bone loss process is increased. The texture index H, follows closely the simulation of architectural changes in that a lower H indicates a greater degree of trabecular bone removal.

VI. DISCUSSION

In this paper, it was not considered necessary to validate the fractal character of our images. Many studies deal with this problem [17]–[27] as well as defining a fractal area. As it can be seen, the H parameter of the fBm permits a clear distinction between different models of the bone structure.

However, this study contains some limitations. The cubes, we used are relatively small leading to only few structural elements in a projection (1–5 structures).

The overlap of surrounding tissues and cortical bone will in practice influence the performance of 2-D descriptors. The data in this study did not contain any surrounding tissue. However, human radii, which are not surrounded by much soft tissue *in situ*, were used for the initial images. Furthermore, as stated in the introduction, the generation of high-quality tomographic X-ray images as those used here requires radiation levels that are not compatible with life.

Projections were constructed numerically such that the actual radiographic process was not exactly simulated. A more realistic setup would be to first obtain X-ray images of the bone samples. This could then be followed by a second step where the cubes are excised for XTM acquisitions and comparison.

Considering the results, high correlations were obtained between the BV/TV, Tb.Th, Tb.Sp, Tb.N, and the H parameter computed for the three orthogonal projections. Different correlations in different directions were obtained which means that

the H parameter is sensitive to the projection direction. Moreover, the same absolute BV/TV gives different H values in projection implying that H may yield more information than just density alone.

VII. Conclusion

This work represents an initial study of trabecular bone on XTM images using fractal analysis. We introduce a tool to erode trabecular bone and simulate bone loss. We were able to demonstrate that detecting trabecular bone changes on XTM projections is feasible. The aim of such investigations is important to find changes in bone structure. This evaluation of trabecular bone architecture may have applications in a variety of tasks of clinical interests. It may be a useful indicator in the early prediction of diseases such as osteoporosis.

Results indicate that the fBm is a robust texture model. It has been validated that fractal attributes on 2-D projections are correlated to simulations of 3-D trabecular bone changes. It remains to more fully understand how 2-D radiographs are linked with projections of 3-D images.

Acknowledgment

The autrhors would like to thank Dr. J. Kinney and D. HAUPT of Lawrence Livermore National Laboratories, and A. Gies for the acquisition of the XTM images. They would also like to thank the anonymous referees for several helpful comments and suggestions.

References

[1] S. R. Cummings, D. M. Black, M. C. Nevitt, W. S. Browner, J. A. Cauley, H. K. Genant, S. R. Mascioli, J. C. Scott, D. G. Jeeley, P. Steiger, and T. M. Vogt, "Appendicular bone density and age predict hip fracture in women," *J. Amer. Med. Assoc.*, vol. 263, pp. 665–668, 1990.

[2] P. D. Ross, J. W. Davis, J. M. Vogel, and R. D. Wasnich, "A critical review of bone mass and the risk of fractures in osteoporosis," *Calcif. Tissue Int.*, vol. 46, pp. 149–161, 1990.

[3] S. A. Goldstein, "The mechanical properties of trabecular bone: Dependence on anatomic location and function," *J. Biomech.*, vol. 20, pp. 1055–1061, 1987.

[4] S. A. Goldstein, R. Goulet, and D. Mc Cubbrey, "Measurement and significance of three-dimensional architecture to the mechanical integrity of trabecular bone," *Calcf. Tissue Int.*, vol. 53, pp. S127–S133, 1993.

[5] S. M. Ott, R. F. Kilcoyne, and C. H. Chesnut, "Ability of our different techniques of measuring bone mass to diagnose vertebral fractures in postmenopausal women," *J. Bone Mineral Res.*, vol. 2, pp. 201–210, 1987.

[6] D. B. Kimmel, R. R. Recker, J. C. Gallagher, A. S. Vaswani, and J. F. Aloia, "A comparison of iliac bone histomorphometric data in postmenopausal osteoporotic and normal subjects," *Bone Mineral*, vol. 11, pp. 217–235, 1990.

[7] H. M. Singh, R. Nagrath, and P. S. Maini, "Changes in the Trabecular patterns of the upper end of the femur as an index of osteoporosis," *J. Bone Joint Surg.*, vol. 52A, pp. 457–467, 1970.

[8] S. Grampp, M. Jergas, C. C. Gluer, P. Lang, P. Brastow, and H. K. Genant, "Radiologic diagnosis of osteoporosis," *Endocrine Radiol.*, vol. 31, no. 5, pp. 1133–1145, Sept. 1993.

[9] L. Benhamou, E. Lespessailles, G. Jacquet, R. Harba, R. Jennane, T. Loussot, D. Tourliere, and W. J. Ohley, "Fractal organization of the trabecular bone images on calcaneus radiographs," *J. Bone Mineral Res.*, vol. 9, pp. 1909–1918, 1994.

[10] S. Majumdar, T. M. Link, X. Ouyang, J. Milard, J. C. Lin, and D. Tsag, "Fractal analysis of radiographs: comparison of techniques and correlation with BMD and biomechanics," *J. Bone Mineral Res.*, vol. 12, p. T652, 1997.

[11] L. A. Feldkamp, S. A. Goldstein, A. M. Parfitt, G. Jesion, and M. Kleerekoper, "The direct examination of three-dimensional bone architecture *in Vitro* by Computed Tomography," *J. Bone Mineral Res.*, vol. 4, pp. 3–11, 1989.

[12] J. A. Hipp, A. Jansujwicz, C. A. Simmons, and B. D. Synder, "Trabecular bone morphology from micro-magnetic resonance imaging," *J. Bone Mineral Res.*, vol. 11, pp. 286–292, 1996.

[13] A. Odgaard, K. Andersen, F. Melsen, and H. J. G. Gundersen, "A direct method for fast three-dimensional serial reconstruction," *J. Microscopy*, vol. 159, pp. 335–342, 1990.

[14] J. H. Kinney, N. E. Lane, and D. L. Haupt, "*In Vivo*, Three-dimensional microscopy of trabecular bone," *J. Bone Mineral Res.*, vol. 10, pp. 264–270, 1995.

[15] B. B. Mandelbrot and J. Van Ness, "Fractional brownian motion, fractional noise and applications," *SIAM*, vol. 10, pp. 422–438, 1968.

[16] R. Jennane, R. Harba, and G. Jacquet, "Quality of synthesis and analysis methods for fractional brownian motion," in *Proc. IEEE Digital Signal Processing Workshop*, Loen, Norway, Sept. 1996, pp. 307–310.

[17] ——, "Estimation de la qualité des méthodes de synthèse du mouvement brownien fractionnaire," *Traitement du Signal*, vol. 13, no. 4, pp. 289–302, 1996.

[18] S. Kay, *Fundamentals of Statistical Signal Processing*. Englewood Cliffs, NJ: Prentice-Hall, 1992.

[19] ——, *Fundamentals of Statistical Signal Processing: Estimation Theory*. Englewood Cliffs, NJ: Prentice-Hall, 1993.

[20] T. Lundahl, W. J. Ohley, S. M. Kay, and R. Siffert, "Fractional brownian motion: a maximum likelihood estimator and its application to image texture," *IEEE Trans. Med. Imag.*, vol. MI-5, no. 3, pp. 152–161, Sept. 1986.

[21] S. Hoefer, H. Hannachi, M. Pandit, and R. Kumaresan, "Isotropic two-dimensional fractional brownian motion and its application in ultrasonic analysis," in *Proc. 14thConf. IEEE Eng. in Med. and Biol. Soc.*, 1992, pp. 1267–1269.

[22] A. P. Pentland, "Fractal-based description of natural scenes," *IEEE Trans. Pattern Anal. Machine Intell.*, vol. PAMI-6, pp. 661–674, Nov. 1984.

[23] J. H. Kinney and M. C. Nicolas, "Xray tomographic microscopy (XTM) using synchrotron radiation," *Annu. Rev. Mater. Sci.*, 1992.

[24] J. Serra, *Image Analysis and Mathematical Morphology*. New York: Academic, 1982, vol. 1.

[25] C. A. Simmons and J. A. Hipp, "Method-based differences in the automated analysis of the three-dimensional morphology of trabecular bone," *J. Bone Mineral Res.*, vol. 12, no. 6, pp. 942–947, 1997.

[26] A. Odgaard and H. J. G. Gundersen, "Quantification of connectivity in cancellous bone, with special emphasis on 3-D reconstructions," *Bone*, vol. 14, pp. 173–182, 1993.

[27] R. Harba, G. Jacquet, R. Jennane, and T. Loussot, "Determination of fractal scales on trabecular bone X-Ray images," *Fractals*, vol. 2, no. 3, pp. 451–456, 1991.